APL Photonics

CMOS-compatible all-dielectric metalens for improving pixel photodetector arrays

Cite as: APL Photonics **5**, 116105 (2020); https://doi.org/10.1063/5.0022162
Submitted: 17 July 2020 • Accepted: 27 October 2020 • Published Online: 13 November 2020

E. Mikheeva, J.-B. Claude, M. Salomoni, et al.

CMOS-compatible all-dielectric metalens for improving pixel photodetector arrays

Cite as: APL Photon. 5, 116105 (2020); doi: 10.1063/5.0022162
Submitted: 17 July 2020 • Accepted: 27 October 2020 •
Published Online: 13 November 2020

E. Mikheeva,[1,2] J.-B. Claude,[1] M. Salomoni,[3,4] J. Wenger,[1] J. Lumeau,[1] R. Abdeddaim,[1] A. Ficorella,[5] A. Gola,[5] G. Paternoster,[5] M. Paganoni,[3] E. Auffray,[4] P. Lecoq,[4,6] and S. Enoch[1,a)]

AFFILIATIONS

[1]Aix Marseille Univ, CNRS, Centrale Marseille, Institut Fresnel, 13013 Marseille, France
[2]Multiwave Imaging, 2 Marc Donadille, 13453 Marseille, France
[3]University of Milano-Bicocca, Piazza dell'Ateneo Nuovo, 1, 20126 Milan, Italy
[4]European Organization for Nuclear Research (CERN), 1211 Geneva, Switzerland
[5]Fondazione Bruno Kessler, Via Santa Croce, 77, 38122 Trento, Italy
[6]Multiwave Metacrystal SA, 34 Route de la Galaise, 1228 Geneva, Switzerland

[a)]**Author to whom correspondence should be addressed:** stefan.enoch@fresnel.fr

ABSTRACT

Metasurfaces and, in particular, metalenses have attracted large interest and enabled various applications in the near-infrared and THz regions of the spectrum. However, the metalens design in the visible range stays quite challenging due to the smaller nanostructuring scale and the limited choice of lossless CMOS-compatible materials. We develop a simple yet efficient design of a polarization-independent, broadband metalens suitable for many CMOS-compatible fabrication techniques and materials and implement it for the visible spectral range using niobium pentoxide (Nb_2O_5). The produced metalens demonstrates high transmittance and focusing ability as well as a large depth of focus, which makes it a promising solution for a new generation of silicon photomultiplier photodetectors with reduced fill factor impact on the performance and reduced electron–hole generation regions, which altogether potentially leads to improved photodetection efficiency and other characteristics.

I. INTRODUCTION

Recent advances in the nanofabrication technology resulted in the enhanced interest to light manipulation with flat nanostructured components—metasurfaces.[1] Due to the high technological potential, the field of metasurfaces was booming during the last decade, resulting in a variety of design ideas and description methods. Besides, metasurfaces keep finding more and more promising applications including miniature integrated devices such as on-chip spectrometers,[2] camera objectives,[3] compact integrated microscopes,[4,5] etc. For many of them, it is of special interest to study wavefront shaping metasurfaces, in particular, metalenses.

Currently, the main metalens designs are based on arrays of nanoparticles and can be roughly classified depending on their size with respect to the wavelength. The first class of metalens use nanoparticles in a resonant regime, which allows for controlling scattering phase varying resonators' shape, size, placement, and composition.[6,7] The second class of metalens employs nanoparticles in an off-resonant sub-wavelength regime. In this case, the metasurface can be described with a locally varying effective refractive index, and focusing is achieved by introducing the geometric phase difference into the beam.[8–10] We further concentrate only on all-dielectric structures as they are known to demonstrate better efficiency.[11] One of the most efficient types of metasurfaces is the Huygen's metasurface based on the mode interference within Mie-resonant high refractive index particles.[12] Although metasurfaces of this type were also designed for a visible domain,[13] the operation wavelength choice is significantly limited by the lack of lossless high-index materials in this range. In addition, due to their resonant nature, these metasurfaces are narrow-band.

On the other hand, devices based on the geometric phase manipulation are advantageous for the broadband operation. The way to design them works with sub-wavelength resonators arranged in a particular way. In the case of devices based on a Berry phase,[14–17] resonators are anisotropic and the phase gradient is introduced by rotating them at a different angle. These metalenses operate only with circularly polarized light, which, however, was shown to be beneficial for broadband imaging applications. For the design of polarization-independent components, resonators are chosen to be symmetric and vary only in size. Although such metasurfaces are described using different formalisms, such as light propagation in fundamental-mode waveguides,[18,19] scattering on sub-wavelength diffraction grating,[20–22] or gradient index (GRIN) surfaces,[23,24] they are all subject to homogenization and can be described with effective parameters (in the case of the Berry phase, the anisotropic effective refractive index is used, and in other cases, the gradient refractive index is used). Most of the suggested options of graded-index metasurfaces are designed with high aspect ratio dielectric posts, which require a complex fabrication process.[14,15,19] In addition, most materials used before are not CMOS-compatible, such as titanium oxide or PMMA, which means that the component cannot be readily integrated into the more complex device.

Here, we develop, fabricate, and characterize a flat metalens design featuring several key advantages. It is fully CMOS-compatible and requires only simple nanostructuring of the surface. The optical performance combines an excellent transmission with focusing on a submicron size spot. Moreover, our metalens is polarization-insensitive, operates over a large spectral bandwidth, and appears to be quite robust to nanofabrication deficiencies. While a similar design was recently introduced in the far infrared region of the spectrum where the fabrication is much easier,[25] here, it is the first time that this approach is demonstrated in the visible spectral range. Our general design can be easily implemented on a large range of applications, notably to improve the photodetection efficiency (PDE) of photodetector arrays, for example, of silicon photomultipliers which are increasingly used as photodetectors in many applications. Focusing the light onto the active region of a photodetector pixel is an efficient approach to reduce the negative impact of the limited fill factor (FF) and improve the photogenerated signal. We focus on a simple design based on the hyperbolic secant profile,[23,25,26] which is one of the perfectly imaging index profiles derived from the Maxwell fish-eye distribution with transformation optics methods.[27] Our metalens design is suitable for many CMOS-compatible fabrication methods and accessible materials. In this work, it is produced with a fabrication process consisting of e-beam vapor deposition and Focused Ion Beam (FIB) milling using the niobium pentoxide Nb_2O_5 material,[28] which has a large transparency window in the optical domain and was earlier used for the ultraviolet metasurface design.[29]

II. RESULTS AND DISCUSSION

The metalens is designed as a 2D square grating of holes of different diameters milled into niobium pentoxide Nb_2O_5. Its refractive index and extinction coefficient measured by spectrophotometry combined with fitting using the Tauc–Lorentz dispersion model are shown in Fig. 1(a). The design of the hole grating is schematically shown in Fig. 1(b), where the overall size is 4 μm and the period is 250 nm. The focusing ability of the metalens is provided by a gradient of the refractive index, which turns the planar incoming wavefront into a focusing spherical wavefront. The refractive index gradient is introduced following the hyperbolic secant distribution equation (1), where n_{eff} is the effective refractive index of the metalens, n_0 is the initial refractive index of the selected material, and x is the varying coordinate,

$$n_{eff}(x) = n_0 \cdot \mathrm{sech}(\alpha x). \tag{1}$$

Parameter α is calculated with Eq. (2), where x_0 defines the lens size (it changes from $-x_0$ to x_0) and n_{x0} is the value of the effective refractive index at the edge of the structure (at $x = x_0$). Although such structures are often designed in the cylindrical coordinates,[23,25] we use the Cartesian system because we aim at applications integrating arrays of metalenses on arrays of pixelized photodetectors, which follow a square lattice,

$$\alpha = \frac{x}{x_0} \cdot \cosh^{-1}\frac{n_0}{n_{x0}}. \tag{2}$$

To introduce the effective index profile, we perforate apertures of a varying diameter $d(x)$ calculated with Eq. (3), where p is the structure period and $F(x)$ is a filling fraction calculated using the Maxwell–Garnett mixing rule adjusted for the dielectric mixtures [Eq. (4)],[30]

$$d(x) = \sqrt{(4/\pi)p^2(1 - F(x))}, \tag{3}$$

$$F(x) = \frac{(n_{eff}(x)^2 - 1)}{(n_{eff}(x)^2 + 1)} \cdot \frac{(n_0^2 + 1)}{(n_0^2 - 1)}. \tag{4}$$

It states that in the case of sub-wavelength inclusions, it is possible to consider the material as a mixture of constituent parts, which in our case is Nb_2O_5 and air. Many homogenization approaches were developed for this type of problem, but this simple technique already provides a sufficiently good description. The resulting effective refractive index profile is shown in Fig. 1(c): the profile calculated analytically with Eq. (1) is shown with a solid line and the actually simulated one is shown with points connected by a dashed line. Minimum aperture size was limited to 100 nm in order to perform fabrication by FIB lithography without requiring to elaborate structures or fabrication. Therefore, in the central part of the lens, there is a mismatch between the ideal and the simulated profile. Once we have the refractive index variation, we select the metalens thickness as $h = 510$ nm, allowing to estimate the phase shift $\phi(r)$ introduced to the transmitted beam [Eq. (5)]. For the chosen operation wavelength $\lambda = 590$ nm (which is a wavelength of operation of a typical silicon photomultiplier that we see as a potential application of this work), the resulting ideal and actual phase profiles are shown together with the refractive index in Fig. 1(c),

$$\phi(r) = \frac{2\pi n(r)h}{\lambda_0}. \tag{5}$$

First of all, the calculated meta-lens was simulated in the CST Studio Suite (r) on an infinite borosilicate glass substrate ($n_{sub} = 1.52$) with a plane wave ($\lambda = 590$ nm) coming at normal incidence. To demonstrate focusing, the XZ-cross section of the normalized intensity in the substrate below the meta-lens is plotted in

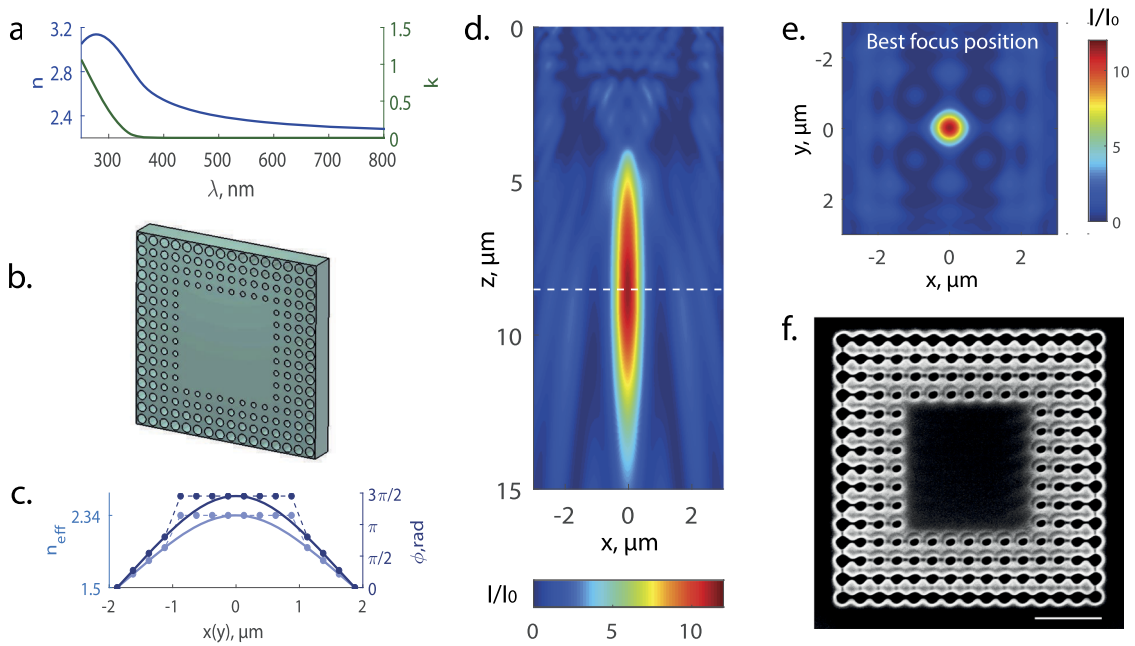

FIG. 1. (a) Refractive index and extinction coefficient of niobium pentoxide (Nb_2O_5) as a function of wavelength. (b) Schematic view of the designed meta-lens—a square lattice with a refractive index gradient introduced by perforating apertures of varying diameters. Only apertures exceeding 100 nm diameter were kept to simplify the fabrication: d = 188 nm, d = 161 nm, d = 134 nm, and d = 109 nm considering the grating period as p = 250 nm. (c) The effective refractive index along the x-horizontal (or y-vertical) direction in (b) is shown in light blue, the solid line shows the profile calculated analytically using Eq. (1), and points joined by the dashed line indicate the actually numerically simulated one. Analytical and numerical phase profiles calculated for the metalens of the thickness h = 510 nm is shown in dark blue. (d) Numerical modeling of the metalens performance. Normalized light intensity in the XZ-plane is shown, and the incident light intensity is used for normalization. The lens is simulated on a glass substrate (n_{sub} = 1.52) with a plane wave of the wavelength λ = 590 nm sent from the vacuum on the top of the image along the z-direction. (e) Normalized light intensity in the XY-plane at the best focus position x = 8.52 μm [the white dashed line in (d)]. (f) The SEM image of the metalens fabricated by FIB-lithography, and the scale bar is 1 μm.

Fig. 1(d). In addition, the XY-cross section corresponding to the best focus position [the white dashed line in Fig. 1(d)] is shown in Fig. 1(e).

The designed metalens was fabricated using a Focused Ion Beam (FIB) milling technique. The Scanning Electron Microscopy (SEM) image of the fabricated structure is shown in Fig. 1(f). Afterward, it was characterized by scanning optical microscopy with the metalens being illuminated from the air side (λ = 570 nm–610 nm) and focusing light in the substrate. For a full characterization, images were taken in several planes. First, images were taken in the XZ-plane [Fig. 2(a)] showing the long focusing spot with the 5.8 μm Full Width at Half Maximum (FWHM) along the propagation direction (which is a large depth of focus). Second, images were taken in the XY-plane [Fig. 2(b)] at the best focus position shown with a white dashed line in Fig. 2(a). The difference between the best focal positions for the simulated [Fig. 1(d)] and measured [Fig. 2(a)] lens can be explained by the overall bias in aperture sizes. Our simulations show that increasing all the aperture sizes in 20% leads to the best focal position shift from ≈8.5 μm to ≈5.7 μm away from the lens.

The images in Figs. 2(a) and 2(b) show that light transmitted through the metalens is focused within a 950 nm by 770 nm spot (4.5% of the total area) with maximum concentration factor $C \approx 5$ defined as the ratio of irradiance on the surface of the concentrator to the irradiance in the detection region,[31] which is equivalent to the ratio of intensities in this case.[32] Slight astigmatism between the X- and Y-axis indicated by the 20% difference in their respective FWHM values is not an effect due to polarization (we use a non-polarized halogen lamp) but is rather connected to the slightly asymmetric shape of the holes milled in the metalens [the SEM image Fig. 1(f)]. Nevertheless, without any post-processing of the image (deconvolution from the microscope point spread function) and despite some nanofabrication imperfections, the focus spot remains below 1 μm^2. Finally, several XY-crosscut images were recorded at several z positions: the best focal positions are $f - 4$ μm, $f + 4$ μm, $f + 6$ μm to fully characterize the propagation, as shown in Fig. 2(c). Altogether, the data in Fig. 2 demonstrate the excellent optical performance of our simple and scalable metalens design. The system is also robust to the minor nanofabrication defects. Contrarily to resonant metasurfaces, our refractive index gradient approach does not require perfect control on each hole size or position. Metalens performance is also illustrated with a video (supplementary material) demonstrating white light (halogen lamp, λ from 500 nm to 650 nm) focusing: the XY-crosscut of the image was taken at different Z-coordinates varying from 0 μm to 15 μm and back. In this video, there are six samples with different milling depths ranging from ≈400 nm deep (on the left) to ≈500 nm (on the right), and the second sample from the right is the metalens shown in Fig. 2. This video confirms the excellent performance of the metalens in the bright field with the spectral range from 500 nm to 650 nm.

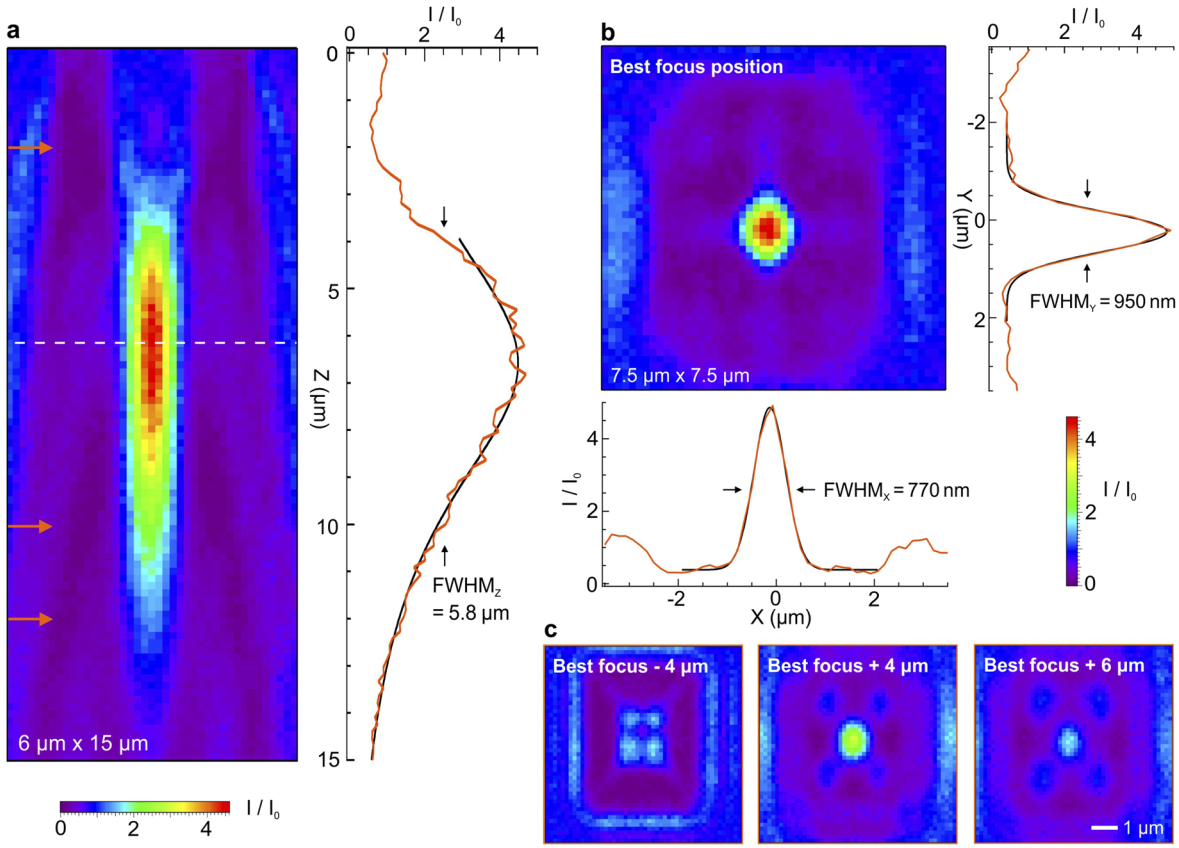

FIG. 2. Experimental characterization of the metalens. (a) Scanning optical microscope image along the XZ-plane parallel to the light propagation. The illumination is provided by a collimated beam from a white lamp spectrally filtered at 590 ± 20 nm incoming from the top of the image. The intensity is normalized by the incoming light intensity in the absence of the structure. The graph on the right shows a crosscut along the vertical direction at the center of the focus. The orange line is the experimental data, and the black line is a fit using a Lorentzian function. (b) Microscope image recorded at the best focus position [the white dashed line in (a)] along the XY-plane perpendicular to the beam propagation. The graphs show crosscuts of the focus spot along the two main directions. Orange lines are the experimental data, while black lines are Gaussian fits used to determine the spot full width at half maximum (FWHM). (c) Images recorded in the transverse plane at different distances from the best focus position [defined in (b)], corresponding to the positions indicated by the orange arrows in (a). All the images in (a)–(c) share the same color scale.

To assess the restrictions induced by the limited minimum size of the holes milled into niobium pentoxide, we model the metalens considering the apertures of diameters $d > 20$ nm [Fig. 3(a) for the XZ-crosscut and Fig. 3(f) for the XY-crosscut]. In this case, the observed focal spot is smaller in comparison to the design with $d > 100$ nm [Figs. 3(b) and 3(g), respectively]. However, due to the choice of the square lattice, a small part of the light is directed away from the focus, which results in the decrease in the intensity enhancement. Therefore, for a given geometry, limitation to sizes bigger than 100 nm does not hamper the optical performance and can even improve slightly the peak intensity at the focus. Then, to study the broadband behavior of the metalens with $d > 100$ nm, it was simulated at several wavelengths such as $\lambda = 490$ nm, 540 nm, 590 nm, 640 nm, and 690 nm. The results [Fig. 3(c)] show that, although the maximum focal spot shifts along the z-direction, the intensity enhancement stays high in the broad wavelength range, and in the case of a photodetection application, the detection region could be placed in such a way that the electron–hole generation probability would be optimal in a large wavelength region.

To estimate the sensitivity to the fabrication error, we simulate the metalens with $d > 100$ nm [Fig. 3(b)] with the aperture diameter taken randomly from the normal distribution with a standard deviation $\sigma = 10$ nm, where the mean value is a calculated diameter for a given spatial point (188 nm, 161 nm, 134 nm, or 109 nm). The results [Fig. 3(d)] show no major decrease in the intensity enhancement, which further demonstrates the design robustness. Then, to analyze the effect of non-verticality of the fabricated apertures, we simulate the metalens using truncated cones instead of the cylinders with perfectly vertical walls—the top base diameter equals to d and the bottom one equals to $0.6d$. Figure 3(e) shows that this leads to a non-negligible decrease in intensity enhancement, which, however, matches better with the measurement results [Fig. 2(a)]. Finally, we simulate the unit cells with the different aperture diameters using periodic boundaries to compute transmittance amplitude

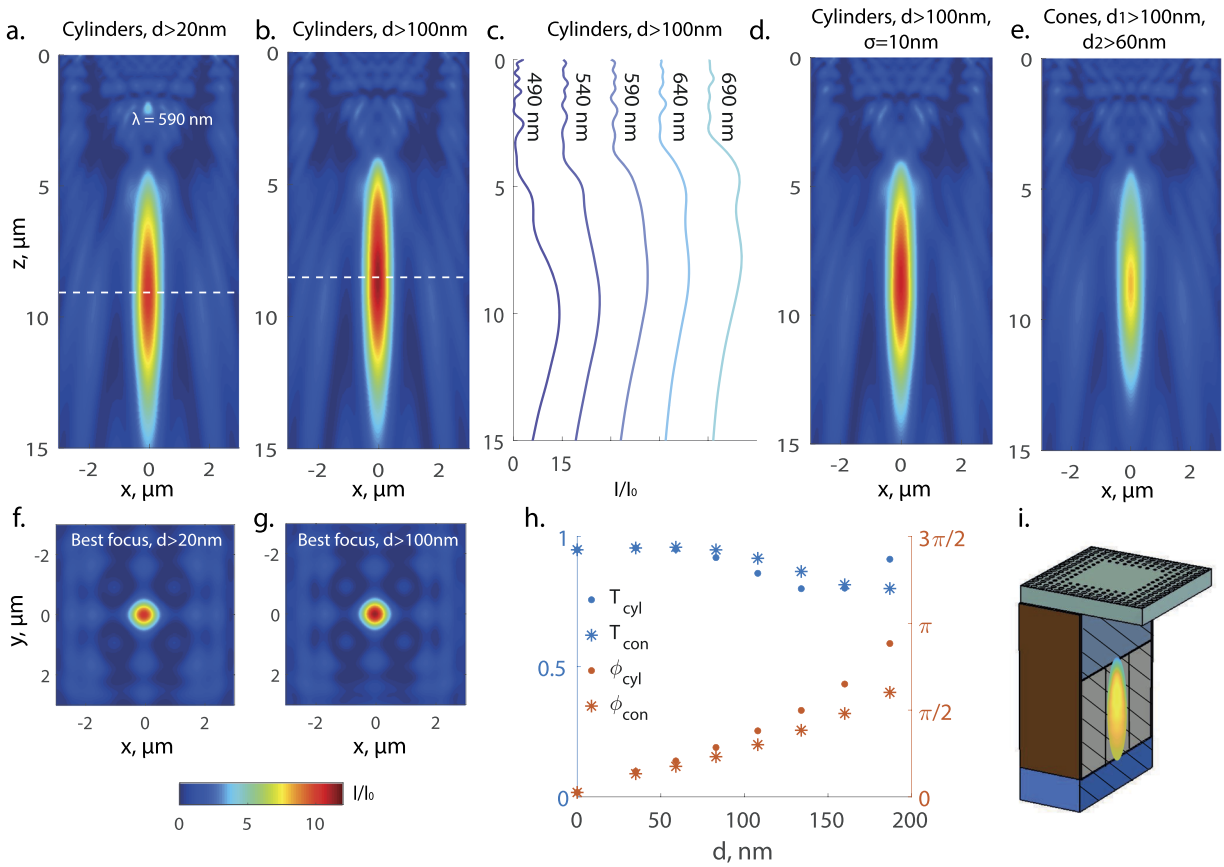

FIG. 3. Metalens numerical modeling (in all cases, n_{sub} = 1.52 and a plane wave is sent from the vacuum on the top of the image along the z-direction). For all the panels of this figure except (c), λ = 590 nm. (a) Normalized light intensity in the XZ-plane for the metalens with aperture diameters d > 20 nm. (b) Normalized light intensity in the XZ-plane for the metalens with aperture diameters d > 100 nm. (c) A crosscut along the vertical direction at the center of the focus corresponding to the simulation made for different wavelengths. The results for λ = 590 nm correspond to the normalized intensity from (b) along the line x = 0. (d) Normalized light intensity in the XZ-plane for the metalens with d > 100 nm, where the diameter is taken randomly from the normal distribution with a mean value d and a standard deviation σ = 10 nm. (e) Normalized light intensity in the XZ-plane for the metalens with truncated cones as apertures—the top base diameter equals to d and the bottom one equals to 60% of d. (f) Normalized light intensity in the XY-plane at the best focus position x = 8.52 μm in the case of design with aperture diameters limited to values d > 20 nm [the white dashed line in (a)]. (g) Normalized light intensity in the XY-plane at the best focus position x = 8.52 μm in the case of d > 100 nm [the white dashed line in (b)]. (h) Numerical simulation of the amplitude and phase of the light transmitted through a periodic metasurface with the apertures of the identical diameter to determine the local response from the different metalens areas. Simulation was done for different diameters d in the case of cylindrical and conical apertures. (i) Illustration of metalens application: reducing the amount of light that would hit the dead boarder of the single photon avalanche photodiode (SPAD) by focusing it in the center of the detection region.

and phase. These two quantities calculated in the case of cylindrical and conical apertures are shown in Fig. 3(h) as a function of the aperture diameter d. The difference in the phase profiles explains the focusing efficiency drop in the case of the conical apertures, which is straightforwardly explained with the homogenization model as well, as it changes mixture proportions and results in a smaller effective refractive index contrast. Moreover, the results shown in Fig. 3(h) allow calculating the average transmittance amplitude, which is $T \approx 0.93$ in the case of cylindrical apertures for both profiles with d > 20 nm and d > 100 nm and in the case of conical ones with d > 100 nm.

To demonstrate the scalability of our design, we investigated the potential of a Fresnel metalens composed of eight different concentric sections (Fig. 4). The purpose of these sections is, as in a regular Fresnel lens, to enable a short focal length together with a large lens diameter without requiring very thick materials. The fabricated Fresnel metalens of dimensions 17 × 17 μm^2 has been characterized with the same method as the metalens in Fig. 2. The optical microscope images taken at the metalens surface and at its best focus plane are shown in Figs. 4(b) and 4(c), respectively. From the axial shift between these two planes, we deduce that this Fresnel metalens has a focal length of 7 μm. Considering the 17 μm dimension of the lens and the 1.5 refractive index of the medium where the light is focused, this Fresnel metalens features an impressive numerical aperture of 1.15. While the concentric sections intrinsic to the Fresnel design introduce interference ripples around the focal spot (as we work under the spatial coherent condition with plane wave illumination), the focal spot still bears transverse

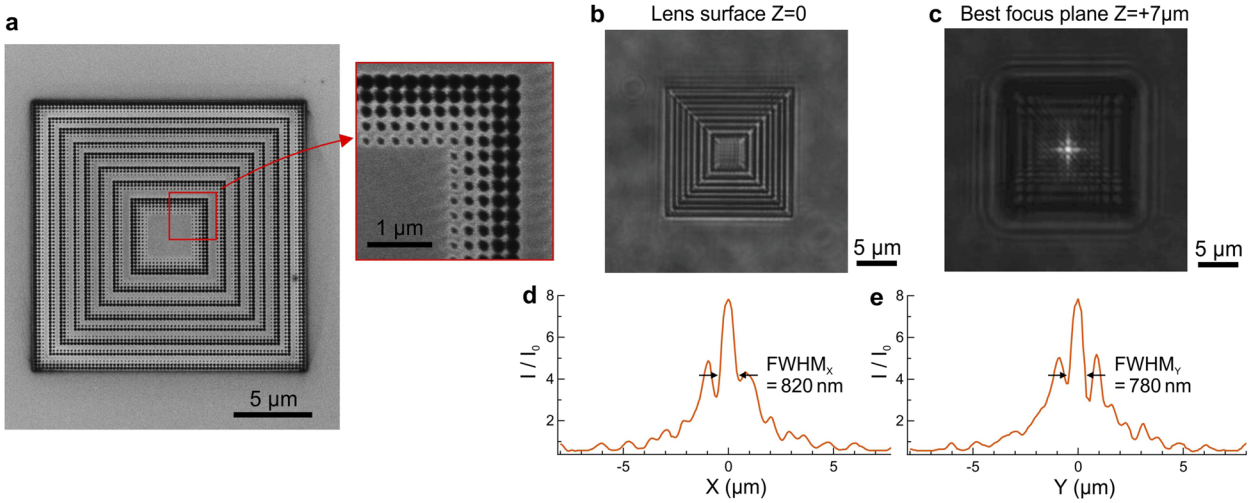

FIG. 4. Fresnel metalens with nanoholes milled in the niobium pentoxide layer. (a) The SEM image of the fabricated sample. Eight different concentric sections are present. The inset shows a high magnification view of one quarter of the central section. (b) Optical microscope image of the Fresnel metalens taken when the microscope focus is set on the Nb_2O_5 layer corresponding to the metalens surface. (c) Optical microscope image taken at the best focus of the metalens, 7 μm below the metalens surface. [(d) and (e)] Crosscuts of the intensity of the image (c) along the x- and y-direction. The intensity is normalized by the light intensity outside the lens [the edge of image (b)].

dimensions well below 1 μm demonstrating efficient focusing. Crosscuts through the focal spot along the horizontal [Fig. 4(d)] and the vertical [Fig. 4(e)] directions indicate better intensity distribution. A local intensity enhancement about 8 together with the FWHM of 800 nm shows the ability of the lens to concentrate light in a tiny spot. Comparing our results with other approaches, high-index microspheres were demonstrated to focus visible and infrared light into spots of approximately one wavelength[33,34] or even half a wavelength[35–37] in FWHM. Besides, silicon cones were used for mid-infrared and long-infrared photodetectors.[38] The solid immersion metalens achieved a FWHM of about 2 λ,[39] while monolithically integrated metalenses also focus infrared light into spots of one wavelength in FWHM.[40] Here, our results achieved in the visible spectral range are at the same level than the state-of-the-art for flat components.

III. CONCLUSIONS

We have developed a polarization-independent broadband efficient metalens and fabricated it with the CMOS-compatible technology. Our results show that the metasurface transmits light with high transmission efficiency (estimated as $T \approx 0.93$), which is then focused on a 950 nm by 770 nm spot occupying ≈4.5% of the total area in the center below it with the fivefold maximum concentration factor reached. The focusing spot is spanning for 5.8 μm in the z-direction, which leaves flexibility for the detection region choice.

The produced metalens can be used for improving the photodetection efficiency (PDE) of silicon photomultipliers by reducing the amount of light that would hit the non-active area at the edge of the single-photon avalanche photodiode (SPAD), which is equivalent to reducing the influence of the fill factor (FF) on the PDE.[40] The situation is illustrated in Fig. 3(i), where the light that was supposed to enter the non-efficient zone close to the border is concentrated at the center of the detection region. Apart from reducing the influence of the FF, focusing light in a small area should allow for creating a smaller electron–hole generation region, which is beneficial for the avalanche generation and signal formation homogeneity. Our metalens design is a step toward ≈100% FF light detection, and it also gives the opportunity to increase the width of the dead border even in very small cells (≤5 μm). This approach is fully scalable and can be easily integrated with any pixelized photodetector array.

IV. METHODS

A. Numerical modeling

All simulations are performed using the commercially available software CST Studio Suite (r). The entire metalens was simulated with the transient solver based on the Finite Integration Technique (FIT). These simulations were done using "open" boundary conditions in the x- and y-direction, which corresponds to a single lens perforated in the infinite film in x- and y-directions. To reduce the computation time, we set the background media to be glass with $n = 1.52$ and artificially fill apertures and the space above the metalens with the vacuum. The excitation source is a plane wave (linearly polarized light with the electric field along the x-direction) coming from the vacuum side, and a field monitor "Power" is set to allow for the extraction of the maximum value of the Poynting vector (P) within one period of time as a function of the coordinate. Finally, we compute the spatial distribution of the transmission coefficient as a ratio between the Poynting vector calculated in the presence and in the absence of the metalens. This method is equivalent to calculating the transmission coefficient as a ratio of field intensities.[32] The unit cell performance as a function of the aperture diameter was simulated using a frequency-domain solver combining the finite element method with special broadband frequency sweep techniques. We used a unit cell boundary condition that considers a

periodic structure and provides a complex transmission coefficient as a result.

B. Nanofabrication

A 510 nm thick layer of Nb_2O_5 was deposited on glass substrates using plasma-assisted electron beam deposition (Bühler SYRUSpro 710). A high density, high uniformity layer was achieved using this technique. The precise thickness was monitored using *in situ* direct optical monitoring (Bühler OMS 5000) at 550 nm. A thin 10 nm additional aluminum layer was deposited on top of the Nb_2O_5 layer using the same technology but unassisted to make the structure conductive and remove electrical charges during etching. The metalens concentrator design used for the numerical simulations was converted using a MATLAB code to generate the pattern compatible with the focused ion beam system (FEI dual-beam DB235 Strata). The pattern was milled using a focused ion beam with a gallium-based source using 30 keV energy and a 10 pA beam current. Scanning electron microscopy images were performed at 5 keV energy with the Schottky Field Emission Gun (SFEG) source of the electron column.

C. Optical characterization

Optical microscopy experiments are based on a home-made microscope system derived from a confocal setup reproducing the conditions used in Ref. 35. The illumination uses the in-built halogen lamp from the Nikon Eclipse inverted microscope. The field and aperture diaphragms are closed to the maximum so that the light beam emerging from the condenser lens illuminating the sample is nearly collimated. The sample containing the metalens is illuminated from the air side, and the apertures milled in niobium pentoxide are filled with air. The characterization of the light focused by the metalens is performed from the borosilicate glass substrate (with the refractive index of the substrate being 1.52). We use a Zeiss C-Apochromat 63 × 1.2NA infinity-corrected water-immersion objective to image the metasurface lens focus. A 30 μm pinhole conjugated with the microscope objective focus plane using a 164 mm Zeiss tube lens defines the confocal detection volume and provides the lateral and axial sectioning. A 3-axis piezo stage (Polytec PI P-517.3CD) scans the sample respective to the fixed detection and illumination. The intensity measurement is performed with an avalanche photodiode (MPD-5CTC, Picoquant) positioned after the pinhole connected to a photon counting module (Hydraharp 400, Picoquant). A bandpass filter (ZET405/488/565/640mv2, Chroma) selects only the light in the 570 nm–610 nm spectral window.

SUPPLEMENTARY MATERIAL

See the supplementary material for *Zscan_whitelamp_subtitles.mp4*: a video demonstrating the white light propagation 15 μm below six metalens samples with varying milling depths.

AUTHORS' CONTRIBUTION

E.M. and S.E. conceived the design, E.M. performed theoretical and numerical calculations, J.L. provided technical support on the materials and coordinated the deposition of the Nb_2O_5 thin film, J.-B.C. fabricated the sample, J.W. characterized the sample, M.S. conceived and planned the Photoquant project, M.S., M.P., P.L., E.A., S.E., and A.G. supervised and coordinated the project, A.F., A.G., and G.P. provided technical support on the photodetector structure and requirements, and E.M. wrote the manuscript with support from J.W., S.E., R.A., J.L., and M.S. All authors provided critical feedback and revised the manuscript.

ACKNOWLEDGMENTS

This work was done in the frame of the project Photoquant, which has received funding from the ATTRACT project funded by the EC under Grant Agreement No. 777222. This project was initiated by the ERC Advanced Grant TICAL (Grant Agreement No. 338953). This project has received funding from the European Research Council (ERC) under the European Union's Horizon 2020 research and innovation program (Grant Agreement No. 723241).

DATA AVAILABILITY

The data that support the findings of this study are available from the corresponding author upon reasonable request.

REFERENCES

[1] S. B. Glybovski, S. A. Tretyakov, P. A. Belov, Y. S. Kivshar, and C. R. Simovski, "Metasurfaces: From microwaves to visible," Phys. Rep. **634**, 1–72 (2016).
[2] A. Leitis, A. Tittl, M. Liu, B. H. Lee, M. B. Gu, Y. S. Kivshar, and H. Altug, "Angle-multiplexed all-dielectric metasurfaces for broadband molecular fingerprint retrieval," Sci. Adv. **5**, eaaw2871 (2019).
[3] A. Arbabi, E. Arbabi, S. M. Kamali, Y. Horie, S. Han, and A. Faraon, "Miniature optical planar camera based on a wide-angle metasurface doublet corrected for monochromatic aberrations," Nat. Commun. **7**, 13682 (2016).
[4] H. Kwon, E. Arbabi, S. M. Kamali, M. Faraji-Dana, and A. Faraon, "Single-shot quantitative phase gradient microscopy using a system of multifunctional metasurfaces," Nat. Photonics **14**, 109–114 (2020).
[5] E. T. F. Rogers, J. Lindberg, T. Roy, S. Savo, J. E. Chad, M. R. Dennis, and N. I. Zheludev, "A super-oscillatory lens optical microscope for subwavelength imaging," Nat. Mater. **11**, 432–435 (2012).
[6] N. Yu and F. Capasso, "Flat optics with designer metasurfaces," Nat. Mater. **13**, 139–150 (2014).
[7] M. Khorasaninejad and F. Capasso, "Metalenses: Versatile multifunctional photonic components," Science **358**, eaam8100 (2017).
[8] P. Lalanne and P. Chavel, "Metalenses at visible wavelengths: Past, present, perspectives," Laser Photonics Rev. **11**, 1600295 (2017).
[9] P. Genevet, F. Capasso, F. Aieta, M. Khorasaninejad, and R. Devlin, "Recent advances in planar optics: From plasmonic to dielectric metasurfaces," Optica **4**, 139 (2017).
[10] S. M. Kamali, E. Arbabi, A. Arbabi, and A. Faraon, "A review of dielectric optical metasurfaces for wavefront control," Nanophotonics **7**, 1041–1068 (2018).
[11] A. I. Kuznetsov, A. E. Miroshnichenko, M. L. Brongersma, Y. S. Kivshar, and B. Luk'yanchuk, "Optically resonant dielectric nanostructures," Science **354**, aag2472 (2016).
[12] M. Decker, I. Staude, M. Falkner, J. Dominguez, D. N. Neshev, I. Brener, T. Pertsch, and Y. S. Kivshar, "High-efficiency dielectric Huygens' surfaces," Adv. Opt. Mater. **3**, 813–820 (2015).
[13] Y. F. Yu, A. Y. Zhu, R. Paniagua-Domínguez, Y. H. Fu, B. Luk' yanchuk, and A. I. Kuznetsov, "High-transmission dielectric metasurface with 2π phase control at visible wavelengths: High-transmission dielectric metasurface with 2π phase control at visible wavelengths," Laser Photonics Rev. **9**, 412–418 (2015).

[14]R. C. Devlin, M. Khorasaninejad, W. T. Chen, J. Oh, and F. Capasso, "Broadband high-efficiency dielectric metasurfaces for the visible spectrum," Proc. Natl. Acad. Sci. U. S. A. **113**, 10473–10478 (2016).
[15]M. Khorasaninejad, W. T. Chen, R. C. Devlin, J. Oh, A. Y. Zhu, and F. Capasso, "Metalenses at visible wavelengths: Diffraction-limited focusing and subwavelength resolution imaging," Science **352**, 1190–1194 (2016).
[16]S. Wang, P. C. Wu, V.-C. Su, Y.-C. Lai, M.-K. Chen, H. Y. Kuo, B. H. Chen, Y. H. Chen, T.-T. Huang, J.-H. Wang, R.-M. Lin, C.-H. Kuan, T. Li, Z. Wang, S. Zhu, and D. P. Tsai, "A broadband achromatic metalens in the visible," Nat. Nanotechnol. **13**, 227–232 (2018).
[17]B. Groever, W. T. Chen, and F. Capasso, "Meta-lens doublet in the visible region," Nano Lett. **17**, 4902–4907 (2017).
[18]S. Vo, D. Fattal, W. V. Sorin, Z. Peng, T. Tran, M. Fiorentino, and R. G. Beausoleil, "Sub-wavelength grating lenses with a twist," IEEE Photonics Technol. Lett. **26**, 1375–1378 (2014).
[19]M. Khorasaninejad, A. Y. Zhu, C. Roques-Carmes, W. T. Chen, J. Oh, I. Mishra, R. C. Devlin, and F. Capasso, "Polarization-insensitive metalenses at visible wavelengths," Nano Lett. **16**, 7229–7234 (2016).
[20]P. Lalanne, S. Astilean, P. Chavel, E. Cambril, and H. Launois, "Design and fabrication of blazed binary diffractive elements with sampling periods smaller than the structural cutoff," J. Opt. Soc. Am. A **16**, 1143 (1999).
[21]A. Zhan, S. Colburn, R. Trivedi, T. K. Fryett, C. M. Dodson, and A. Majumdar, "Low-contrast dielectric metasurface optics," ACS Photonics **3**, 209–214 (2016).
[22]M. Ye, Y. Peng, and Y. S. Yi, "Silicon-rich silicon nitride thin films for subwavelength grating metalens," Opt. Mater. Express **9**, 1200 (2019).
[23]T.-M. Chang, S. Guenneau, J. Hazart, and S. Enoch, "Focussing light through a stack of toroidal channels in PMMA," Opt. Express **19**, 16154 (2011).
[24]P. R. West, J. L. Stewart, A. V. Kildishev, V. M. Shalaev, V. V. Shkunov, F. Strohkendl, Y. A. Zakharenkov, R. K. Dodds, and R. Byren, "All-dielectric subwavelength metasurface focusing lens," Opt. Express **22**, 26212 (2014).
[25]J. Moughames, S. Jradi, T. M. Chan, S. Akil, Y. Battie, A. E. Naciri, Z. Herro, S. Guenneau, S. Enoch, L. Joly, J. Cousin, and A. Bruyant, "Wavelength-scale light concentrator made by direct 3D laser writing of polymer metamaterials," Sci. Rep. **6**, 33627 (2016).
[26]N. Kundtz and D. R. Smith, "Extreme-angle broadband metamaterial lens," Nat. Mater. **9**, 129–132 (2010).
[27]K. Mantel, D. Bachstein, and U. Peschel, "Perfect imaging of hypersurfaces via transformation optics," Opt. Lett. **36**, 199 (2011).
[28]W. Cote, M. Slocum, S. Chandra, M. Fredell, and T. Rahmlow, "Optical properties, morphology and temperature influence of SiO_2, Nb_2O_5 and HfO_2 films as a function of ion energy and process," in *Optical Interference Coatings* (Optical Society of America, 2016), p. ThC-7.
[29]K. Huang, J. Deng, H. S. Leong, S. L. K. Yap, R. B. Yang, J. Teng, and H. Liu, "Ultraviolet metasurfaces of ≈80% efficiency with antiferromagnetic resonances for optical vectorial anti-counterfeiting," Laser Photonics Rev. **13**, 1800289 (2019).
[30]A. Sihvola, "Mixing rules with complex dielectric coefficients," Subsurf. Sens. Technol. Appl. **1**, 393–415 (2000).
[31]S. Donati, G. Martini, and M. Norgia, "Microconcentrators to recover fill-factor in image photodetectors with pixel on-board processing circuits," Opt. Express **15**, 18066 (2007).
[32]H. A. Macleod, *Thin-Film Optical Filters*, Series in Optics and Optoelectronics, 4th ed. (CRC Press; Taylor & Francis, Boca Raton, FL 2010), Vol. 26, pp. 18–20, 26.
[33]K. W. Allen, F. Abolmaali, J. M. Duran, G. Ariyawansa, N. I. Limberopoulos, A. M. Urbas, and V. N. Astratov, "Increasing sensitivity and angle-of-view of mid-wave infrared detectors by integration with dielectric microspheres," Appl. Phys. Lett. **108**, 241108 (2016).
[34]F. Abolmaali, A. Brettin, A. Green, N. I. Limberopoulos, A. M. Urbas, and V. N. Astratov, "Photonic jets for highly efficient mid-IR focal plane arrays with large angle-of-view," Opt. Express **25**, 31174–31185 (2017).
[35]P. Ferrand, J. Wenger, A. Devilez, M. Pianta, B. Stout, N. Bonod, E. Popov, and H. Rigneault, "Direct imaging of photonic nanojets," Opt. Express **16**, 6930 (2008).
[36]B. S. Luk'yanchuk, R. Paniagua-Domínguez, I. Minin, O. Minin, and Z. Wang, "Refractive index less than two: Photonic nanojets yesterday, today and tomorrow," Opt. Mater. Express **7**, 1820–1847 (2017).
[37]A. Maslov and V. Astratov, "Resolution and reciprocity in microspherical nanoscopy: Point-spread function versus photonic nanojets," Phys. Rev. Appl. **11**, 064004 (2019).
[38]B. Jin, G. W. Bidney, A. Brettin, N. I. Limberopoulos, J. M. Duran, G. Ariyawansa, I. Anisimov, A. M. Urbas, S. D. Gunapala, H. Li, and V. N. Astratov, "Microconical silicon mid-ir concentrators: Spectral, angular and polarization response," Opt. Express **28**, 27615–27627 (2020).
[39]S. Zhang, A. Soibel, S. A. Keo, D. Wilson, S. B. Rafol, D. Z. Ting, A. She, S. D. Gunapala, and F. Capasso, "Solid-immersion metalenses for infrared focal plane arrays," Appl. Phys. Lett. **113**, 111104 (2018).
[40]F. Li, J. Deng, J. Zhou, Z. Chu, Y. Yu, X. Dai, H. Guo, L. Chen, S. Guo, M. Lan, *et al.*, "HgCdTe mid-infrared photo response enhanced by monolithically integrated meta-lenses," Sci. Rep. **10**, 1–10 (2020).